Time Reversal Imaging by Adaptive Interference Canceling

José M.F. Moura and Yuanwei Jin

Abstract

We develop the *Time Reversal Adaptive Interference Canceler* (TRAIC) time reversal beamformer (TRBF), a new algorithm to detect and locate targets in rich scattering environments. It utilizes time reversal in two stages: (1) *Anti*-focusing: TRAIC time reverses and then reshapes the clutter backscatter to *mitigate* the clutter response; (2) *Focusing*: TRBF time reverses the residual backscatter to *focus* the radar image on the target. Laboratory experiments with electromagnetic radar data in a highly cluttered environment confirm the superiority of TRAIC-TRBF over conventional direct subtraction beamform imaging.

Index Terms

Time Reversal, Wideband Radar Imaging, Adaptive Interference Cancelation, Waveform Shaping, Super-Resolution

Edics: SAM-IMGA, SAM-APPL

I. Introduction

Locating and imaging targets buried in high clutter poses considerable challenges. Detection and imaging algorithms suffer significant performance loss because the channel Green's function is very different from the direct path model that these algorithms usually assume. In complex channels, for example, when the propagation speed profile is spatially varying or due to boundary layers, the use of numerical codes that integrate the wave equation, like matched field processing (MFP) in underwater acoustics, e.g., [1], provides the channel Green's function. But MFP is prohibitively expensive in most applications and is highly sensitive to accurate knowledge of the environmental conditions. This paper

The authors are with the Department of Electrical and Computer Engineering, Carnegie Mellon University, Pittsburgh, PA, USA 15213 (e-mail: {moura,ywjin}@ece.cmu.edu); ph: (412)268-6341; fax: (412)268-3890.

This work is funded by the Mathematical Time Reversal Methods Program, DSO-CMP, Defense Advanced Research Projects Agency (DARPA), through the Army Research Office under grant no. W911NF-04-1-0031.

explores how time reversal (TR) can be used in *localizing* targets in highly cluttered environments. References [2], [3], [4], [5], [6] have shown the power of time reversal to *focus* with super-resolution on a source in a highly dispersive medium by time reversing and retransmitting the time dispersed signal received at an array of sensors. References [7], [8] demonstrate super-resolution focusing in underwater acoustics and reference [9] demonstrates focusing in the electromagnetic domain. Focusing results from the time reversibility of the wave equation in a non-absorbing medium: the highly dispersed back-propagated field is time reversed, resent, and focuses on the radiating source. The more inhomogeneous the media is, the higher the focusing resolution achieved. Intuitively, time reversal is equivalent to generating a *virtual aperture* larger than its actual physical size, yielding a much higher resolution. Beyond focusing, recent work on time reversal imaging includes Lehman and Devaney [10], Devaney [11], Prada and Thomas [12], Borcea et al. [13], [14], and other references [15], [16], [17]. In these works, the Multiple Signal Classification (MUSIC) algorithm is combined with time reversal for locating well resolved targets, where the MUSIC spectrum is constructed by eigen-decomposing the so called time reversal matrix. This approach is applicable only when the number of scatterers in the imaged area is smaller than the number of antennas since the generalized MUSIC spectrum requires that the number of scatterers be smaller than the number of antennas.

In [18], we studied detection with time reversal. We showed for the electromagnetic (EM) domain that time reversal provides significant gains when detecting targets burried in clutter using a single sensor. In this paper, we consider localization of targets in high clutter for radar (electromagnetic) data, which we also refer to as imaging. We present a new high resolution time-reversal imaging algorithm, the *Time Reversal Adaptive Interference Canceler* (TRAIC) followed by time reversal beamforming (TRBF). Unlike time reversal MUSIC based algorithms, TRAIC-TRBF only requires the number of antennas to be larger than the number of potential targets, regardless of the number of scatterers in the illuminated region. The TRAIC algorithm *reshapes* the time reversed backscatter from the clutter to minimize the energy returns from the clutter at the array. In contrast with *focusing*, the goal of TRAIC is *anti*-focusing, i.e., nulling the EM energy received at the transmit/receive radar backscattered by the clutter. Probing the cluttered environment with the reshaped time reversed waveform enhances the backscatter from the target. The second stage, TRBF, time reverses the backscatter from the target and resends it into the medium to focus on the target. The high resolution achieved at this stage by time reversal generates a narrow beam, which provides high resolution in localization and imaging.

Physical and mathematical time reversal. We describe time reversal in the paper as if the signals were physically time reversed and retransmitted. In practice, in many situations, there is no need to actually physically retransmit the time reversed signals—in this case, the time reversal steps in TRAIC-TRBF

become algorithmic steps with no need for additional signal retransmission. When time reversal is used as an algorithmic step, with no physical retransmission of the signals, we refer to it as mathematical time reversal.

Notation. We use lower case boldface letters to denote vectors and upper case boldface letters to denote matrices. In addition, we adopt the following conventions throughout the paper, $(\cdot)^*$ for conjugate; $(\cdot)^T$ for transpose; $(\cdot)^H$ for Hermitian transpose; $\mathrm{diag}[\mathbf{x}]$ for the diagonal matrix whose diagonal is the vector $\mathbf{x}$; $\|\cdot\|$ for the vector (matrix) Frobenius norm; $\mathbf{I}_m$ for the identity matrix of order m; $\det(\mathbf{A})$ for the determinant of matrix $\mathbf{A}$; and the inner product notation $\langle \mathbf{x}, \mathbf{y} \rangle = \mathbf{x}^H \mathbf{y}$.

II. Data Model

We present in this section the data model that we adopt. Subsection II-A discusses a stepped frequency synthesis of the transmitted signals, subsection II-B the array configuration, and subsection II-C the multi-static response matrix and the time reversal matrix.

A. Stepped frequency synthesis

The illuminating signal $s(t)$, $t \in [0 \;\; T]$, has Fourier transform $S(\omega)$, $\omega \in [\omega_0 \;\; \omega_0 + B]$. The signal has duration T and bandwidth B. Time reversal of a real valued signal is simply phase conjugation in the frequency domain, i.e., the Fourier transform of $s(-t)$ is $S^*(\omega)$ (see Oppenheim and Willsky, [19].) In practice, for realizable signals with finite duration T, the realizable version of the time reversed signal follows by delaying by T the time reversed signal, which introduces a phase shift in the frequency domain. We ignore this phase shift in the sequel.

Real time synthesis in the time domain of the signal $s(t)$ at the radar frequencies of interest requires expensive instrumentation. In section IV, these cost considerations lead us, instead, to synthesizing by a stepped frequency approach the transmitted signals, e.g., Wehner [20] and Mahafza [21]. In this paper, we transmit a series of bursts of narrow band pulses where each burst is a sequence of Q pulses stepped (shifted) in frequency from pulse to pulse by a fixed frequency step size $\Delta\omega$. The Q monochromatic signals sample uniformly the wideband signal spectrum $S(\omega)$ at the frequencies

$$\forall 0 \le q \le Q-1: \qquad \omega_q = \omega_0 + q\Delta\omega, \tag{1}$$

where we choose

$$\omega_0 = \frac{2\pi}{T(Q-1)} q_1, \quad q_1 \text{ an integer} \tag{2}$$

$$\Delta\omega = \frac{\omega_{Q-1} - \omega_0}{Q-1}, \tag{3}$$

which leads to

$$\forall 0 \leq q \leq Q-1: \qquad \omega_q = \frac{2\pi}{T(Q-1)}(q_1+q). \tag{4}$$

Care must be taken when sampling a signal in the frequency domain. Uniformly sampling by $\Delta\omega$ the signal bandwidth B, replicates the original signal in the time domain,

$$\widetilde{s}(t) = \frac{1}{\Delta\omega}\sum_n s\left(t - \frac{2\pi}{\Delta\omega}n\right). \tag{5}$$

To avoid overlapping the time domain replicas of duration T, the frequency sampling should be dense enough, i.e., upper bounded as

$$\Delta\omega = \frac{B}{Q-1} \leq \frac{2\pi}{T}.$$

B. Array configuration

We adopt the multi-static configuration shown on the left of Fig. 1. The scene is in the (x, y)-plane and the region of interest is partitioned into a finite number of pixels in range and cross range. The imaging radar in Fig. 1 has a pair of antenna arrays A and B located along the y-axis: $A = (A_0, \cdots, A_{P-1})$ with P antennas and $B = (B_0, \cdots, B_{N-1})$ with N antennas. The right of Fig. 1 shows the experimental

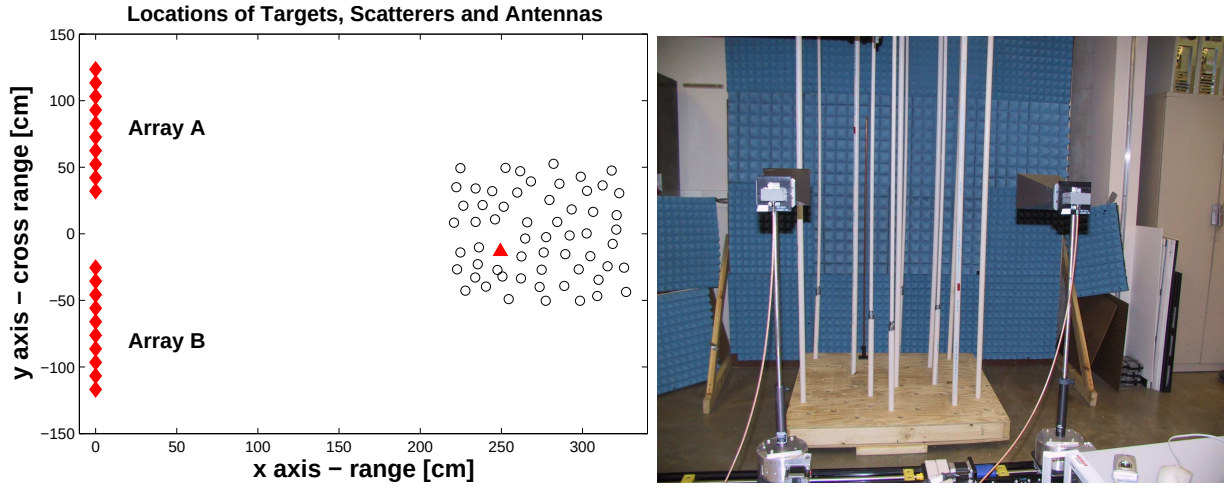

Fig. 1. Left: Multi-static array configuration for time reversal imaging. Antenna arrays A and B are placed along the y-axis. The x-axis denotes the range direction; the y-axis denotes the cross range direction. Right: Experimental setup used in Section IV for time reversal measurements. Two horn antennas, mounted on two rails, move to synthesize a uniform linear array. The scatterers ($\circ$) are a mixture of copper and solid dielectric pipes. The targets ($\triangle$) are copper rods. The scattering and targets are mounted on a wood platform.

set-up used in Section IV. Two horn antennas are mounted on rails and move to synthesize uniform linear arrays. The scatterers and the targets are mounted on a platform.

C. Multi-static Response Matrix and Time Reversal Matrix

We introduce in this section two matrices that play an important role in time reversal techniques: the multi-static response matrix and the time reversal matrix.

Multi-static Response Matrix $\mathbf{K}(\omega_q)$. With respect to Fig. 1, let $k(\omega_q; B_n \leftarrow A_p)$ denote the frequency response of the propagation channel between the p-th transmit antenna A_p and the n-th receive antenna B_n at the discrete angular frequency ω_q. We organize the total of NP channel responses into the $N \times P$ *multi-static response matrix* $\mathbf{K}(\omega_q)$ at frequency ω_q (e.g., Lehman and Devaney, [10], [22],and Chambers, [23].) We now determine the structure of this matrix in terms of the Green's functions characterizing the media propagation between antennas and scattering centers or targets. We consider first the single target case in a highly cluttered environment. The case of multiple targets follows by superposition of all the target reflections, neglecting secondary scattering between targets.

Single target. Let $\mathbf{x}_t$, $\mathbf{r}_{B_n}$, and $\mathbf{r}_{A_p}$ denote the locations of the target, of the n-th antenna B_n of array B, and of the p-th antenna A_p of array A, respectively. The (n,p)-th entry of $\mathbf{K}(\omega_q)$ is:

$$[\mathbf{K}(\omega_q)]_{n,p} = k(\omega_q; B_n \leftarrow A_p), \tag{6}$$

$$= G(\mathbf{r}_{B_n}, \mathbf{x}_t; \omega_q)\tau(\mathbf{x}_t; \omega_q)G(\mathbf{x}_t, \mathbf{r}_{A_p}; \omega_q), \tag{7}$$

where: $\tau(\mathbf{x}_t; \omega_q)$ is the complex reflectivity of the point target at location $\mathbf{x}_t$, and $G(\mathbf{r}, \mathbf{r}'; \omega_q)$ is the Green's function of the background medium between locations $\mathbf{r}'$ and $\mathbf{r}$ at frequency ω_q. In signal frequency terms, the Green's function is the channel response at location $\mathbf{r}$ to an impulse at location $\mathbf{r}'$. Often, the Green's function satisfies the *reciprocity relation*:

$$G(\mathbf{r}, \mathbf{r}'; \omega_q) = G(\mathbf{r}', \mathbf{r}; \omega_q). \tag{8}$$

We assume that the medium is reciprocal and that (8) holds. An example of a Green's function, is the 'background' or free space Green's function, [24], [25],

$$G(\mathbf{r}, \mathbf{r}'; \omega_q) = \frac{1}{4j} H_0^{(2)}(k_q|\mathbf{r} - \mathbf{r}'|), \tag{9}$$

where $H_0^{(2)}$ is the zeroth-order Hankel function of the second kind, $k_q = \omega_q/c$ is the wavenumber of a propagating wave with angular frequency ω_q, and c is the medium propagation velocity. In the near field, the free space Green's function can be approximated as

$$G\left(\mathbf{r}, \mathbf{r}'; \omega_q\right) \approx -\sqrt{\frac{1}{8\pi k_q}} \frac{e^{-jk_q|\mathbf{r}-\mathbf{r}'|}}{|\mathbf{r} - \mathbf{r}'|}, \quad \text{for} \quad \left|\mathbf{r} - \mathbf{r}'\right| > 3\lambda. \tag{10}$$

In the far field, the Green's function is simply a delay

$$G\left(\mathbf{r}, \mathbf{r}'; \omega_q\right) \approx e^{-jk_q|\mathbf{r}-\mathbf{r}'|}. \tag{11}$$

The "direct path" Green's functions hold under the Born approximation, or weak scattering condition, and in general does not hold when multiple scattering is non-negligible. For a discussion on the Born approximation and the multiple scattering Foldy-Lax approximation in the context of time reversal imaging, readers can refer to [15], [16], [17], [26].

We first consider the receiving array to be at points $\mathbf{r}_{B_i}$, $i = 0, \cdots, N-1$. Stacking the Green's functions $G(\mathbf{r}_{B_i}, \mathbf{x}_t; \omega_q)$ from the target $\mathbf{x}_t$ to each of the array elements B_i, $i = 0, \cdots, N-1$, into an N-dimensional vector, define the receive array response vector at array B for a target at $\mathbf{x}_t$ as:

$$\mathbf{g}_B(\mathbf{x}_t; \omega_q) = \left[G(\mathbf{r}_{B_0}, \mathbf{x}_t; \omega_q), \cdots, G\left(\mathbf{r}_{B_{N-1}}, \mathbf{x}_t; \omega_q\right)\right]^T. \tag{12}$$

In the far field, and for a linear equi-spaced array, $\mathbf{g}_B(\mathbf{x}_t; \omega_q)$ reduces to the N-dimensional conventional steering vector

$$\mathbf{g}_B(\mathbf{x}_t; \omega_q) \approx \left[1, e^{-j2\pi \frac{d}{\lambda_q}\sin\theta}, \cdots, e^{-j2\pi \frac{d(N-1)}{\lambda_q}\sin\theta}\right]^T, \tag{13}$$

where: θ is the azimuth angle, and d is the inter-element spacing.

Similar to Eqn. (12), the P-dimensional transmit array response vector is

$$\mathbf{g}_A(\mathbf{x}_t; \omega_q) = \left[G(\mathbf{x}_t, \mathbf{r}_{A_0}; \omega_q), \cdots, G\left(\mathbf{x}_t, \mathbf{r}_{A_{P-1}}; \omega_q\right)\right]^T. \tag{14}$$

Applying Eqns. (12) and (14) to (7) yields a revealing subspace representation of the $N \times P$ response matrix $\mathbf{K}(\omega_q)$:

$$\mathbf{K}(\omega_q) = \tau(\mathbf{x}_t; \omega_q)\, \mathbf{g}_B(\mathbf{x}_t; \omega_q)\, \mathbf{g}_A^T(\mathbf{x}_t; \omega_q). \tag{15}$$

Multiple targets. In general, if there are M well resolved targets, and neglecting in this discussion the secondary scattering among targets, the target response matrix is the superposition of the individual target responses given by (15), i.e.,

$$\begin{aligned} \mathbf{K}(\omega_q) &= \sum_{m=1}^{M} \tau(\mathbf{x}_{t,m}; \omega_q) \mathbf{g}_B(\mathbf{x}_{t,m}; \omega_q) \mathbf{g}_A^T(\mathbf{x}_{t,m}; \omega_q), & (16) \\ &= \mathbf{G}_B(\omega_q)\, \mathbf{\Pi} \mathbf{G}_A(\omega_q), & (17) \end{aligned}$$

where $\mathbf{\Pi}$ is the diagonal matrix of target reflectances $\tau(\mathbf{x}_{t,m}; \omega_q)$, and the $N \times M$ matrix $\mathbf{G}_B(\omega_q)$ and the $P \times M$ matrix $\mathbf{G}_A(\omega_q)$ collect the array response vectors in (12) and (14) for the array B and the array A, respectively,

$$\begin{aligned} \mathbf{\Pi} &= \mathrm{diag}\left[\tau(\mathbf{x}_{t,1}; \omega_q), \cdots, \tau(\mathbf{x}_{t,M}; \omega_q)\right], \\ \mathbf{G}_B(\omega_q) &= \left[\mathbf{g}_B(\mathbf{x}_{t,1}; \omega_q), \cdots, \mathbf{g}_B(\mathbf{x}_{t,M}; \omega_q)\right], \\ \mathbf{G}_A(\omega_q) &= \left[\mathbf{g}_A(\mathbf{x}_{t,1}; \omega_q), \cdots, \mathbf{g}_A(\mathbf{x}_{t,M}; \omega_q)\right]. \end{aligned} \tag{18}$$

Time Reversal Matrix $\mathbf{T}(\omega_q)$. The *time reversal matrix*, e.g, [5], [4], is

$$\forall 0 \leq q \leq Q-1: \quad \mathbf{T}(\omega_q) = \mathbf{K}^T(\omega_q)\,\mathbf{K}^*(\omega_q).$$

Clutter and Target Multi-static Response Matrices. In the paper, we distinguish between the following three multi-static response matrices: the clutter channel multi-static response matrix $\mathbf{K}_c(\omega_q)$ when only scatterers are present; the clutter plus target channel multi-static response matrix $\mathbf{K}_{c+t}(\omega_q)$ when both scatterers plus target are present; and the target channel multi-static response matrix

$$\mathbf{K}_t(\omega_q) = \mathbf{K}_{c+t}(\omega_q) - \mathbf{K}_c(\omega_q). \tag{19}$$

As an abuse of terminology, we will simply refer to these matrices as the scatterers or clutter channel response, the clutter plus target channel response, and the target channel response, respectively.

The structure of $\mathbf{K}_c(\omega_q)$ and $\mathbf{K}_t(\omega_q)$ follows Eqn. (7), i.e.,

$$[\mathbf{K}_c(\omega_q)]_{n,p} = k_c(\omega_q; B_n \leftarrow A_p) \tag{20}$$

$$[\mathbf{K}_t(\omega_q)]_{n,p} = k_t(\omega_q; B_n \leftarrow A_p), \tag{21}$$

where $k_c(\omega_q; B_n \leftarrow A_p)$ and $k_t(\omega_q; B_n \leftarrow A_p)$ are the clutter and target responses between antennas A_p and B_n, respectively.

III. TRAIC-TRBF: Mathematical Description

In this section, we describe a time reversal based algorithm to image targets in rich scattering scenes—the time reversal adaptive interference canceler time reversal beamformer (TRAIC-TRBF); see also preliminary work in [27]. We start by clarifying the terminology. In many radar applications, and in this paper, *imaging* means roughly constructing a soft version of an occupancy grid map of a region of interest (ROI), which is sampled by a finite number of grid cells, or pixels.

To image a target in high density clutter, we could attempt to locate the clutters and then use these data in the Green's function of the channel to model the secondary scattering from the clutter to the target and determine the position of the target—mimicking in a sense matched field processing. This approach suffers from the burden of having to locate accurately the clutter positions. For example, narrowband MUSIC requires that the number of sensors in the array be larger than the number of clutters. In heavy clutter, this is not the case and techniques like these have limited applicability. With TRAIC-TRBF, we adopt a different strategy. We avoid all together the step of locating the clutters. Instead, we time reverse the clutter returns and reshape this time reversed waveform so that, after retransmission, we minimize (*null* or *cancel*) the clutters' backscatter received at the array. This strategy mitigates the clutter response and reinforces the return from the target. The clutter mitigation stage is followed by a second stage of

time reversal that focuses the retransmitted signal on the target, with little backscatter to the array from the scatterers. In other words, we first time reverse and reshape to *anti-focus* on the clutter, and then we time reverse the returns to *focus* on the target. Because the backscatter from the clutter is reduced by TRAIC-TRBF, we do not need a sophisticated propagation model and a simple direct path is usually sufficient to locate the target.

We now present formally the time reversal adaptive interference canceler time reversal beamforming (TRAIC-TRBF) algorithm. It is designed to image (locate) targets in highly dense cluttering environments. As mentioned, it performs two tasks, clutter mitigation and target focusing, through a series of transmission and processing steps. There are a total of five steps: clutter channel probing; time reversal waveform reshaping for clutter cancellation; target channel monitoring; time-reversal target focusing; and, finally, image formation by beamforming and triangulation. The first three steps constitute TRAIC, while the two last steps are the TRBF. The first two steps of TRAIC learn the clutter channel and construct a whitening filter for clutter mitigation. This allows us to subtract out the clutter component in each of the three subsequent steps. Step 3 monitors the target channel, step 4 time reverses the returns from the reshaped target waveform to focus on the target, and step 5 uses beamforming and triangulation to form the image. TRAIC-TRBF uses time reversal twice—first, to adaptively *anti-focus*, null or cancel, the clutter; second, to *focus* on the target.

Subsection III-A details TRAIC-TRBF. Subsection III-B derives the weight vectors used to beamform the data in step 4. Subsection III-C presents an alternative imager, the TRAIC-TR MUSIC, where we combine TRAIC and TR with MUSIC. This algorithm is compared to TRAIC-TRBF in Section IV.

A. TRAIC-TRBF

Time reversal is usually associated with focusing. To mitigate the effect of clutter, we take here the opposite point of view: We reshape the time reversed signal to achieve anti-focus, i.e., to null or to cancel, the backscatter from the clutter. Thus, the goal becomes to reshape the time reversed clutter returns to synthesize a waveform that, once retransmitted through the same medium, minimizes the energy of the clutter returns. In this subsection, we detail the five steps represented of the time reversal adaptive interference cancellation (TRAIC) time reversal beamformer (TRBF) algorithm (TRAIC-TRBF). In the sequelae, we recall that the symbols $\mathbf{K}_c(\omega_q)$, $\mathbf{K}_{c+t}(\omega_q)$, and $\mathbf{K}_t(\omega_q)$ represent the $N \times P$ response matrices of the clutter, the clutter plus target, and the target at frequency ω_q, respectively.

Step 1: Clutter channel probing (A→B). This is the training step in which there exist only scatterers. The goal of this step is to estimate very reliably from the received data the clutter channel frequency response $\mathbf{K}_c(\omega_q)$. This stage assumes that only clutter and no targets are present. This is realistic in many

applications where one can survey the area of interest before it becomes active. We first consider, without loss of generality, that the probing signal is transmitted from antenna A_p and received at the N sensors of array B; by reversing the argument, we obtain similar results when the signal is first transmitted from the sensors at B and received by the P sensors at A. Each antenna A_p is individually excited and radiates monochromatic signals with frequencies ω_q, $q = 0, \cdots, Q-1$, one frequency at a time. The scattered returns from the signal transmitted from antenna A_p at frequency ω_q are received at antennas B_n, $n = 0, \cdots, N-1$, and collected in the N-dimensional array B received signal vector $\mathbf{r}_p(\omega_q)$. We assume that the probing step can be repeated several times to average out possible measurement noise, i.e., we assume that we have $m = 1, \cdots, M$ noisy snapshots

$$\mathbf{r}_{p,m}(\omega_q) = \mathbf{K}_c(\omega_q)\,\mathbf{e}_p S(\omega_q) + \mathbf{n}_m(\omega_q),\ m = 1, \cdots, M, \tag{22}$$

where $\mathbf{e}_p$ is the vector whose p-th entry is 1 and 0 elsewhere and $\mathbf{n}_m(\omega_q)$ is additive noise. From these M snapshots, we can estimate accurately the clutter channel frequency response. For example, for white Gauss noise, taking $S(\omega_q) = 1$, $q = 0, \cdots, Q-1$, we get that the p-th column of $\mathbf{K}_c(\omega_q)\,\mathbf{e}_p$ is estimated by

$$\widehat{\mathbf{K}}_c(\omega_q)\,\mathbf{e}_p = \frac{1}{M}\sum_{m=1}^{M}\mathbf{r}_{p,m}(\omega_q) \approx \mathbf{K}_c(\omega_q)\,\mathbf{e}_p. \tag{23}$$

We repeat this process for all the antennas A_p, $p = 0, \cdots, P-1$, which leads to estimates of the P columns of $\mathbf{K}_c(\omega_q)$. From this clutter channel probing step, we conclude that

$$\widehat{\mathbf{K}}_c(\omega_q) \approx \mathbf{K}_c(\omega_q)$$

and so the clutter channel frequency response can be safely assumed to be accurately determined by step 1.

Step 2: Waveform reshaping for clutter cancellation. The signals received by array B scattered by the clutter in step 1 are widely spread in time. Intuitively, if we time reverse these signals and retransmit them from B, they will focus on the clutters—this is the common goal of time reversal. To image in a highly cluttered environment, we propose an alternative goal for time reversal. Rather than focusing, we reshape the time reversed signals so that they *avoid* the clutters, once retransmitted from B. We refer to this as clutter *nulling* or clutter *cancellation*. This is the goal of step 2 and we explain it now.

We first time reverse the backscattered signals at array B. As mentioned before, apart a time delay, this corresponds to phase conjugation in the frequency domain. Then, we reshape and energy normalize the time reversed backscatter. This is achieved by a reshaping filter, which at frequency ω_q is represented by the $N \times N$ matrix $\mathbf{W}(\omega_q)$. The reshaped signal vector transmitted from array B is

$$\forall 0 \le p \le P-1: \qquad \mathbf{x}_p(\omega_q) = \mathbf{W}(\omega_q)\,\mathbf{K}_c^*(\omega_q)\,S^*(\omega_q)\,\mathbf{e}_p. \tag{24}$$

The clutter backscatter received at antenna array A is

$$\forall 0 \leq p \leq P-1: \quad \mathbf{y}_p(\omega_q) = \mathbf{K}_c^T(\omega_q)\,\mathbf{x}_p, \tag{25}$$

$$= \mathbf{K}_c^T(\omega_q)\,\mathbf{W}(\omega_q)\,\mathbf{K}_c^*(\omega_q)\,S^*(\omega_q)\,\mathbf{e}_p. \tag{26}$$

Stacking the P vector signals received by all the P antennas of array A given by (26), we get

$$\mathbf{y}(\omega_q) = \begin{bmatrix} \mathbf{y}_0(\omega_q) \\ \vdots \\ \mathbf{y}_{P-1}(\omega_q) \end{bmatrix}. \tag{27}$$

Stacking these vectors $\{\mathbf{y}(\omega_q)\}$ for all the Q frequencies into the single vector $\mathbf{y}$ yields

$$\mathbf{y} = \begin{bmatrix} \mathbf{y}(\omega_0) \\ \vdots \\ \mathbf{y}(\omega_{Q-1}) \end{bmatrix}. \tag{28}$$

We design the reshaping filters $\{\mathbf{W}(\omega_q), q = 0, \cdots, Q-1\}$ by minimizing the total energy of the vector $\mathbf{y}$ (given by its squared norm or Frobenius norm)

$$\|\mathbf{y}\|_F^2 = \sum_{q=0}^{Q-1} \|\mathbf{K}_c^T(\omega_q)\,\mathbf{W}(\omega_q)\,\mathbf{K}_c^*(\omega_q)\|_F^2 |S(\omega_q)|^2. \tag{29}$$

Given the additive nature of this cost function, we minimize each of its terms, which leads to

$$\mathbf{W}(\omega_q)_{\text{opt}} = \arg\min \|\mathbf{K}_c^T(\omega_q)\,\mathbf{W}(\omega_q)\,\mathbf{K}_c^*(\omega_q)\|_F^2. \tag{30}$$

We solve this design problem subject to the following constraints:

1) **Unit norm:** $\|\mathbf{W}(\omega_q)\|_F^2 = 1, \forall \omega_q$. This avoids the trivial solution $\mathbf{W}(\omega_q) = 0$ and biasing it towards any of the Q frequencies ω_q.
2) **Symmetry:** $\mathbf{W}(\omega_q) = \mathbf{W}(\omega_q)^H > \mathbf{0}, \forall \omega_q$, i.e., $\mathbf{W}(\omega_q)$ is Hermitian and positive definite (or semi-definite if $\mathbf{K}_c(\omega_q)$ is rank deficient.) The time reversal matrix $\mathbf{K}_c^T(\omega_q)\,\mathbf{K}_c^*(\omega_q)$ becomes now the time reversal *anti-focusing* matrix

   $$\mathbf{K}_c^T(\omega_q)\,\mathbf{W}(\omega_q)\,\mathbf{K}_c^*(\omega_q)$$

   To preserve the Hermitian positive definiteness (or semi-definiteness if $\mathbf{K}_c^T(\omega_q)$ is rank deficient) of the time reversal anti-focusing matrix, we choose our solution $\mathbf{W}(\omega_q)$ to be symmetric and positive definite.
3) **Constant volume:** $\prod_{i=1}^N w_{ii}(\omega_q)$ is constant. Geometrically, for a matrix $\mathbf{A}$, $|\det[\mathbf{A}]|$ is the volume of the n-dimensional parallelepiped whose generating edges are given by the rows (or columns) of the $n \times n$ matrix $\mathbf{A}$. This volume is the largest when the generating edges are orthogonal, and, in this

case, the volume is the product of the lengths of the edges, [28], [29]. By Hadamard's inequality, [29], $|\mathbf{W}(\omega_q)| \leq \prod_{i=1}^{N} w_{ii}(\omega_q)$, where $\mathbf{W}(\omega_q) = [w_{ij}(\omega_q)]$. We consider this as an alternative constraint to constraining $\det[\mathbf{W}(\omega_q)]$. We will see that this condition facilitates the derivation of the reshaping filter.

Condition (1) constrains the reshaping to have finite, nonzero, normalized energy. Condition (3) is more subtle, it is like an entropy based design. While the goal is to avoid the clutters, because we do not know where they are, we still want to illuminate uniformly as much as possible the space where the target may possibly be, and that is precisely what an entropy design accomplishes—maximum uncertainty, like with a uniform distribution.

The following two results determine the reshaping filter $\mathbf{W}(\omega_q)$: Result 1 is for $N \leq P$, while Result 2 is for $N > P$.

Result 1: Assume $N \leq P$ and $\mathbf{K}_c(\omega_q)$, $\forall q$, is full rank. Let

$$\mathbf{K}_c(\omega_q) = \mathbf{U}_q \widetilde{\mathbf{\Lambda}}_q \mathbf{V}_q^H \tag{31}$$

be the singular value decomposition (SVD) of $\mathbf{K}_c(\omega_q)$, where

$$\widetilde{\mathbf{\Lambda}}_q = \begin{bmatrix} \mathbf{\Lambda}_q & \mathbf{0}_{N\times(P-N)} \end{bmatrix}, \tag{32}$$

$$\mathbf{\Lambda}_q = \operatorname{diag}[\lambda_{q,1}, \cdots, \lambda_{q,N}]. \tag{33}$$

The optimal reshaping filter (30) under conditions (1) through (3) above is

$$\mathbf{W}(\omega_q)_{\text{opt}} = k_q \mathbf{U}_q^* \mathbf{\Lambda}_q^{-2} \mathbf{U}_q^T, \tag{34}$$

$$= k_q \left[\mathbf{K}_c^*(\omega_q)\, \mathbf{K}_c^T(\omega_q)\right]^{-1}, \tag{35}$$

where k_q is

$$k_q^2 = \left(\sum_{i=1}^{N} \frac{1}{\lambda_{q,i}^4}\right)^{-1}, \tag{36}$$

$$= \left(\left\| \left(\mathbf{K}_c^*(\omega_q)\, \mathbf{K}_c^T(\omega_q)\right)^{-1} \right\|_F^2\right)^{-1}. \tag{37}$$

Proof: From the SVD (31) of $\mathbf{K}_c(\omega_q)$ it follows successively

$$\begin{aligned}
\left\|\mathbf{K}_c^T(\omega_q)\,\mathbf{W}(\omega_q)\mathbf{K}_c^*(\omega_q)\right\|_F^2 &= \left\|\mathbf{V}_q^*\widetilde{\mathbf{\Lambda}}_q\mathbf{U}_q^T\mathbf{W}(\omega_q)\,\mathbf{U}_q^*\widetilde{\mathbf{\Lambda}}_q\mathbf{V}_q^T\right\|_F^2, && (38)\\
&= \left\|\mathbf{\Lambda}_q\underbrace{\mathbf{U}_q^T\mathbf{W}(\omega_q)\,\mathbf{U}_q^*}_{\mathbf{F}}\mathbf{\Lambda}_q\right\|_F^2, && (39)\\
&= \|\mathbf{\Lambda}_q\mathbf{F}\mathbf{\Lambda}_q\|_F^2, && (40)\\
&= \sum_{i=1}^{N}\lambda_{q,i}^4|f_{ii}|^2+\sum_i\sum_{j,i<j}\lambda_{q,i}\lambda_{q,j}\left(|f_{ij}|^2+|f_{ji}|^2\right). && (41)
\end{aligned}$$

Since $\mathbf{F}$ is Hermitian and positive definite, this implies that

$$\begin{aligned}
\forall 1\le i\le N:\ \ f_{ii} &> 0, && (42)\\
\forall j:\ \ \lambda_{q,j} &> 0. && (43)
\end{aligned}$$

Hence, $\|\mathbf{\Lambda}_q\mathbf{F}\mathbf{\Lambda}_q\|_F^2$ is minimized by $\{f_{ij}=0, i\neq j\}$, which yields

$$\mathbf{F}=\mathrm{diag}[f_{11},\cdots,f_{NN}]. \tag{44}$$

Next, we determine the values of f_{ii}. Recall the inequality between the arithmetic and geometric means

$$\sum_{i=1}^{n}a_i\ge n\sqrt[n]{\prod_{i=1}^{n}a_i}, \tag{45}$$

whenever $a_1,\cdots,a_n>0$, with equality holding when $a_1=a_2=\cdots=a_n$ and $\prod_{i=1}^n a_i$ is a constant. Using now condition (3), we derive that for (41) and using (45)

$$\begin{aligned}
\|\mathbf{\Lambda}_q\mathbf{F}\mathbf{\Lambda}_q\|_F^2 &= \sum_{i=1}^{N}\lambda_{q,i}^4f_{ii}^2, && (46)\\
&\ge N\sqrt[N]{\prod_{i=1}^{N}\lambda_{q,i}^4f_{ii}^2}, && (47)\\
&= N\sqrt[N]{\left(\prod_{i=1}^{N}\lambda_{q,i}^4\right)\det[\mathbf{W}(\omega_q)]}. && (48)
\end{aligned}$$

The equality holds when

$$\forall 1\le i\le N:\ \ \lambda_{q,i}^4f_{ii}^2=k_q^2, \tag{49}$$

or

$$\forall 1\le i\le N:\ \ f_{ii}=\frac{k_q}{\lambda_{q,i}^2}. \tag{50}$$

By condition (1), we have

$$k_q^2 = \left(\sum_{i=1}^{N} \frac{1}{\lambda_{q,i}^4} \right)^{-1} = \left(\left\| \left[\mathbf{K}_c^* \left(\omega_q \right) \mathbf{K}_c^T \left(\omega_q \right) \right]^{-1} \right\|_F^2 \right)^{-1}. \tag{51}$$

This leads to the solution

$$\mathbf{W} \left(\omega_q \right)_{\text{opt}} = k_q \mathbf{U}_q^* \mathbf{\Lambda}_q^{-2} \mathbf{U}_q^T. \tag{52}$$

If we allow an arbitrary unitary transform matrix in the above equation, we then find that this solution can be further written in a compact and revealing form as

$$\mathbf{W} \left(\omega_q \right)_{\text{opt}} = k_q \left[\mathbf{K}_c^* \left(\omega_q \right) \mathbf{K}_c^T \left(\omega_q \right) \right]^{-1}. \tag{53}$$

■

Result 2: Assume that $N > P$ or that $\mathbf{K}_c \left(\omega_q \right)$ is rank deficient, i.e., $1 \leq r = \text{rank} \left[\mathbf{K}_c \left(\omega_q \right) \right] \leq P$. Let

$$\mathbf{K}_c \left(\omega_q \right) = \mathbf{U}_q \widetilde{\mathbf{\Pi}}_q \mathbf{V}_q^H$$

be the singular value decomposition of $\mathbf{K}_c \left(\omega_q \right)$, where

$$\widetilde{\mathbf{\Pi}}_q = \begin{bmatrix} \mathbf{\Pi}_q & \mathbf{0}_{r \times (P-N)} \\ \mathbf{0}_{(N-r) \times r} & \mathbf{0}_{(N-r) \times (P-N)} \end{bmatrix}, \tag{54}$$

$$\mathbf{\Pi}_q = \text{diag} \left[\lambda_{q,1}, \cdots, \lambda_{q,r} \right]. \tag{55}$$

Then, under conditions (1) through (3),

$$\mathbf{W} \left(\omega_q \right)_{\text{opt}} = k_q \mathbf{U}_q^* \mathbf{\Phi}_{q,r}^2 \mathbf{U}_q^T \tag{56}$$

$$= k_q \left[\mathbf{K}_c^* \left(\omega_q \right) \mathbf{K}_c^T \left(\omega_q \right) \right]^{\dagger}, \tag{57}$$

where † denotes pseudo-inverse, and

$$\mathbf{\Phi}_{q,r} = \text{diag} \left[\frac{1}{\lambda_{q,1}}, \cdots, \frac{1}{\lambda_{q,r}}, \underbrace{0, \cdots, 0}_{(N-r)} \right], \tag{58}$$

$$k_q^2 = \left(\sum_{i=1}^{r} \frac{1}{\lambda_{q,i}^4} \right)^{-1} = \left(\left\| \left(\mathbf{K}_c^* \left(\omega_q \right) \mathbf{K}_c^T \left(\omega_q \right) \right)^{\dagger} \right\|_F^2 \right)^{-1}. \tag{59}$$

Proof: From

$$\left\|\mathbf{K}_c^T(\omega_q)\,\mathbf{W}(\omega_q)\,\mathbf{K}_c^*(\omega_q)\right\|_F^2 = \left\|\mathbf{V}_q^*\widetilde{\mathbf{\Pi}}_q\mathbf{U}_q^T\mathbf{W}(\omega_q)\,\mathbf{U}_q^*\widetilde{\mathbf{\Pi}}_q\mathbf{V}_q^T\right\|_F^2, \tag{60}$$

$$= \left\|\widetilde{\mathbf{\Pi}}_q\underbrace{\mathbf{U}_q^T\mathbf{W}(\omega_q)\,\mathbf{U}_q^*}_{\mathbf{F}}\widetilde{\mathbf{\Pi}}_q\right\|_F^2, \tag{61}$$

$$= \left\|\widetilde{\mathbf{\Pi}}_q\mathbf{F}\widetilde{\mathbf{\Pi}}_q\right\|_F^2, \tag{62}$$

$$= \sum_{i=1}^{r}\lambda_{q,i}^4|f_{ii}|^2+\sum_i\sum_{j,i<j}\lambda_{q,i}\lambda_{q,j}\left(|f_{ij}|^2+|f_{ji}|^2\right). \tag{63}$$

Notice that $\mathbf{F}$ is Hermitian and positive semi-definite. Minimizing the left hand side of Eqn. (63) and using condition (3) and inequality (45) yields

$$\forall 1\le i\le r: \quad f_{ii}=\frac{k_q}{\lambda_{q,i}^2}. \tag{64}$$

Therefore, the shaping filter takes the form:

$$\mathbf{W}(\omega_q)_{\text{opt}} = k_q\mathbf{U}_q^*\text{diag}\left[\frac{1}{\lambda_{q,1}^2},\cdots,\frac{1}{\lambda_{q,r}^2},\underbrace{0,\cdots,0}_{(N-r)}\right]\mathbf{U}_q^T, \tag{65}$$

$$= k_q\left[\mathbf{K}_c^*(\omega_q)\,\mathbf{K}_c^T(\omega_q)\right]^\dagger, \tag{66}$$

which is Eqn. (59) in Result 2. ■

We now interpret the solutions (35) or (57) in the next Result. First, recall the projection operator on the column space of matrix $\mathbf{A}$

$$\mathbf{P}_{\mathbf{A}}=\mathbf{A}(\mathbf{A}^H\mathbf{A})^{-1}\mathbf{A}^H.$$

Result 3: The reshaped signal $\mathbf{x}_p(\omega_q)$ and the clutter returns $\mathbf{y}_p(\omega_q)$, $p=0,\cdots,P-1$, given by (24) and (26), respectively, when the reshaping filter $\mathbf{W}(\omega_q)$ is given by Result 2, see (57), are

$$[\mathbf{x}_0(\omega_q)\cdots\mathbf{x}_{P-1}(\omega_q)] = k_q\left[\mathbf{K}_c^*(\omega_q)\,\mathbf{K}_c^T(\omega_q)\right]^{-1}\mathbf{K}_c^*(\omega_q)\,S^*(\omega_q), \tag{67}$$

$$[\mathbf{y}_0(\omega_q)\cdots\mathbf{y}_{P-1}(\omega_q)] = k_q\mathbf{P}_{\mathbf{K}_c^T(\omega_q)}S(\omega_q). \tag{68}$$

In particular, if $P=N$ and $\mathbf{K}_c(\omega_q)$ is full rank, see Result 1 and (35), we have

$$[\mathbf{x}_0(\omega_q)\cdots\mathbf{x}_{P-1}(\omega_q)] = k_q\mathbf{K}_c^{-T}(\omega_q)\,S^*(\omega_q), \tag{69}$$

$$[\mathbf{y}_0(\omega_q)\cdots\mathbf{y}_{P-1}(\omega_q)] = k_q\mathbf{I}S(\omega_q). \tag{70}$$

Proof: By direct substitution of (57) in (24) and (26), Eqns. (67) and (68) follow.

When $P=N$ and $\mathbf{K}_c(\omega_q)$ is full rank, Eqn. (69) follows directly from (67). Also, we have that

$$\mathbf{K}_c^T(\omega_q)\,\mathbf{W}(\omega_q)\,\mathbf{K}_c^*(\omega_q)=k_q\mathbf{I}, \tag{71}$$

which leads to (70). ■

Result 3 shows that the reshaped time reversed signal designed for clutter mitigation unscrambles the clutter channel response: note that, in the first step, we transmit from a single antenna from array A, say antenna 1, and receive the clutter returns at all antennas at array B. We then, time reverse the signal received at each antenna in array B and retransmit simultaneously from all these antennas at array B. If the clutter is very rich, these signals should focus at antenna 1 at array A, from which it was transmitted initially. The filter $\mathbf{W}(\omega_q)$ forces this to happen—the signal refocus at antenna 1 of array A and is zero at every other antenna at A. The clutter response can then be subtracted out in succeeding processing steps. Intuitively, the filters $\mathbf{W}(\omega_q), \forall q$, after the clutter response is subtracted out, reduce the imaged area to an open field, i.e., with no clutter, so that subsequent processing can assume that target only is present. We can then image the area using a simple Green's function, without requiring knowledge of the position of the scatterers.

Step 3: Target channel monitoring. (B→A) In this step, the environment is probed with the signal (67). Targets may be present or absent. The "signal plus clutter components" in the received signal (if a target is present) are

$$\begin{aligned} \mathbf{z}'_p(\omega_q) &= \left(\mathbf{K}_t(\omega_q) + \mathbf{K}_c(\omega_q)\right)^T \mathbf{x}_p(\omega_q), && (72)\\ &= \mathbf{z}^t_p(\omega_q) + \mathbf{z}^c_p(\omega_q), && (73)\\ &= k_q\left(\mathbf{K}^T_t(\omega_q)\mathbf{K}^{-T}_c(\omega_q) + \mathbf{I}\right)\mathbf{e}_p S^*(\omega_q), && (74) \end{aligned}$$

where in (74) we assumed that $N = P$ and $\mathbf{K}_c(\omega_q)$ is full rank. We subtract out the known component $\mathbf{z}^c_p(\omega_q)$ due to the clutter. The resulting data matrix $\mathbf{Z}(\omega_q)$ is

$$\begin{aligned} \mathbf{Z}(\omega_q) &= \left[\mathbf{z}^t_0(\omega_q), \mathbf{z}^t_1(\omega_q), \cdots, \mathbf{z}^t_{P-1}(\omega_q)\right], && (75)\\ &= k_q\mathbf{K}^T_t(\omega_q)\mathbf{K}^{-T}_c(\omega_q)S^*(\omega_q). && (76) \end{aligned}$$

Step 4: Time reversal target focusing. (A→B) The returns from step 3, received at the antennas in array A, after the whitened clutter has been subtracted out, are either noise or target response plus noise. The target response may be smeared out by the complex environment, e.g., multiple scattering from clutter to target. The goal of step 4 is to obtain focused returns from the target by time reversing the returns from step 3, retransmitting them into the environment, and collecting back the returns at array B.

The "signal plus clutter components" of the received signal at B are (again, assuming a target is present)

$$\begin{aligned}
\mathbf{p}'_p(\omega_q) &= [\mathbf{K}_t(\omega_q) + \mathbf{K}_c(\omega_q)][\mathbf{z}_p(\omega_q)]^* && (77)\\
&= [\mathbf{K}_t(\omega_q) + \mathbf{K}_c(\omega_q)]\, k_q \mathbf{K}_t^H(\omega_q)\, \mathbf{K}_c^{-H}(\omega_q)\, \mathbf{e}_p S(\omega_q) && (78)\\
&= k_q \mathbf{K}_t(\omega_q)\, \mathbf{K}_t^H(\omega_q)\, \mathbf{K}_c^{-H}(\omega_q)\, \mathbf{e}_p S(\omega_q) \\
&\quad + k_q \mathbf{K}_c(\omega_q)\, \mathbf{K}_t^H(\omega_q)\, \mathbf{K}_c^{-H}(\omega_q)\, \mathbf{e}_p S(\omega_q) && (79)\\
&= \mathbf{p}_p^t(\omega_q) + \mathbf{p}_p^c(\omega_q), && (80)
\end{aligned}$$

where the target component is given by

$$\begin{aligned}
\mathbf{p}_p^t(\omega_q) &= \mathbf{p}'_p(\omega_q) - \mathbf{p}_p^c(\omega_q), && (81)\\
&= k_q \mathbf{K}_t(\omega_q)\, \mathbf{K}_t^H(\omega_q)\, \mathbf{K}_c^{-H}(\omega_q)\, \mathbf{e}_p S(\omega_q). && (82)
\end{aligned}$$

Grouping $\mathbf{p}_p^t(\omega_q)$, $p = 0, \cdots, P-1$, into an $N \times N$ matrix $\mathbf{M}^B$, yields the clutter focused target response matrix measured at array B

$$\begin{aligned}
\mathbf{M}^B(\omega_q) &= \left[\mathbf{p}_0^t(\omega_q), \mathbf{p}_1^t(\omega_q), \cdots, \mathbf{p}_{P-1}^t(\omega_q)\right], && (83)\\
&= k_q \mathbf{K}_t(\omega_q)\, \mathbf{K}_t^H(\omega_q)\, \mathbf{K}_c^{-H}(\omega_q)\, S(\omega_q). && (84)
\end{aligned}$$

Note that $\mathbf{M}^B(\omega_q)$ collects the returns resulting from the two steps, target channel monitoring (step 3) and time reversal target focusing (step 4), when we start from array B in step 3.

Similarly, if we repeat steps 3 and 4 but starting initially from the antennas in array B, we obtain the clutter target response matrix measured at array A given by the $P \times P$ matrix

$$\mathbf{M}^A(\omega_q) = k_q \mathbf{K}_t^T(\omega_q)\, \mathbf{K}_t^*(\omega_q)\, \mathbf{K}_c^{-*}(\omega_q)\, S(\omega_q). \quad (85)$$

Step 5: Image formation. This final step forms the image by scanning the area of interest with two focused beams, one at array B and the other at array A. The beam at B is when we start at B and end at B; similarly, the beam at A is when we start at A and end at A.

Start with the returns $\mathbf{M}^B(\omega_q)$ and $\mathbf{M}^A(\omega_q)$. Let $\mathbf{w}_{rB}(\mathbf{x};\omega_q)$, $\mathbf{w}_{tB}(\mathbf{x};\omega_q)$, $\mathbf{w}_{rA}(\mathbf{x};\omega_q)$, and $\mathbf{w}_{tA}(\mathbf{x};\omega_q)$ denote the receive and transmit beams for arrays B and A, respectively, at frequency $\omega_q, \forall q$. Their structures are presented in the next Subsection III-B. The complex output of the beamformers B and A are

$$\begin{aligned}
Y^B(\mathbf{x};\omega_q) &= \mathbf{w}_{rB}^H(\mathbf{x};\omega_q)\, \mathbf{M}^B(\omega_q)\, \mathbf{w}_{tB}(\mathbf{x};\omega_q), && (86)\\
Y^A(\mathbf{x};\omega_q) &= \mathbf{w}_{rA}^H(\mathbf{x};\omega_q)\, \mathbf{M}^A(\omega_q)\, \mathbf{w}_{tA}(\mathbf{x};\omega_q). && (87)
\end{aligned}$$

We now combine the outputs of these two beamformers by triangulation, i.e., we multiply the outputs of the two beamformers at each frequency to form the final image $I(\mathbf{x})$ as the spatial distribution of the total energy at each pixel $\mathbf{x}$

$$I(\mathbf{x}) = \sum_{q=0}^{Q-1} \left| Y^A(\mathbf{x};\omega_q)\, Y^B(\mathbf{x};\omega_q) \right|^2 . \tag{88}$$

Eqn. (88) implements the *energy detector.*[1]

B. Weight vectors

We design the imaging weight vectors introduced in Subsection III-A by maximizing $I(\mathbf{x})$ given in (88) subject to unit norm constraints on the weight vectors as explained here. Using the subspace revealing representation (15) for the response matrices, and from Eqns. (84), (85), and (88), we obtain

$$\begin{aligned} I(\mathbf{x}) &= \sum_{q=0}^{Q-1} \left| \mathbf{w}_{rB}^H(\mathbf{x};\omega_q)\, \mathbf{M}^B(\omega_q)\, \mathbf{w}_{tB}(\mathbf{x};\omega_q) \right|^2 \left| \mathbf{w}_{rA}^H(\mathbf{x};\omega_q)\, \mathbf{M}^A(\omega_q)\, \mathbf{w}_{tA}(\mathbf{x};\omega_q) \right|^2 \qquad (89) \\ &= \sum_{q=0}^{Q-1} \left| \langle \mathbf{w}_{rB}(\mathbf{x};\omega_q), \mathbf{g}_B(\mathbf{x};\omega_q) \rangle \right|^2 \left\| \mathbf{g}_A(\mathbf{x};\omega_q) \right\|^2 \left| \langle \mathbf{w}_{tB}(\mathbf{x};\omega_q), \mathbf{K}_c^{-1}(\omega_q)\, \mathbf{g}_B(\mathbf{x};\omega_q) \rangle \right|^2 \\ &\quad \times \left| \langle \mathbf{w}_{rA}(\mathbf{x};\omega_q), \mathbf{g}_A(\mathbf{x};\omega_q) \rangle \right|^2 \left\| \mathbf{g}_B(\mathbf{x};\omega_q) \right\|^2 \left| \langle \mathbf{w}_{tA}(\mathbf{x};\omega_q), \mathbf{K}_c^{-T}(\omega_q)\, \mathbf{g}_A(\mathbf{x};\omega_q) \rangle \right|^2 \\ &\quad \times k_q^4 \left| S(\omega_q) \right|^4 \left| \tau(\mathbf{x};\omega_q) \right|^8 \qquad (90) \end{aligned}$$

In (90), we indicate explicitly the target reflectivity $\tau(\mathbf{x};\omega_q)$. Given the additivity of $I(\mathbf{x})$ in (90), the weight vectors, which are frequency dependent, can be calculated frequency by frequency. For a unit target impulse response at $\mathbf{x}_t = \mathbf{x}$, the optimal weights are obtained by the following optimization

$$\{\mathbf{w}_{rB}(\mathbf{x};\omega_q), \mathbf{w}_{tB}(\mathbf{x};\omega_q), \mathbf{w}_{rA}(\mathbf{x};\omega_q), \mathbf{w}_{tA}(\mathbf{x};\omega_q)\} \Big|_{\text{opt}} = \arg \max_{\text{weights}} I(\mathbf{x}) \Big|_{\mathbf{x}_t = \mathbf{x}} , \tag{91}$$

subject to the constraints

$$\|\mathbf{w}_{rB}(\mathbf{x};\omega_q)\|^2 = \|\mathbf{w}_{tB}(\mathbf{x};\omega_q)\|^2 = \|\mathbf{w}_{rA}(\mathbf{x};\omega_q)\|^2 = \|\mathbf{w}_{tA}(\mathbf{x};\omega_q)\|^2 = 1. \tag{92}$$

The solution is promptly found as an application of Schwartz inequality and is in the following Result.

[1]The energy detector is a generalized likelihood ratio test for this problem, see [18]. The matched filter is not applicable since the target channel response is assumed to be unknown.

Result 4: The optimal weights (91) under the unit norm constraint (92) are

$$\mathbf{w}_{rB}\left(\mathbf{x};\omega_q\right) = \frac{\mathbf{g}_B\left(\mathbf{x};\omega_q\right)}{\left\|\mathbf{g}_B\left(\mathbf{x};\omega_q\right)\right\|}, \tag{93}$$

$$\mathbf{w}_{tB}\left(\mathbf{x};\omega_q\right) = \frac{\mathbf{K}_c^{-1}\left(\omega_q\right)\mathbf{g}_B\left(\mathbf{x};\omega_q\right)}{\left\|\mathbf{K}_c^{-1}\left(\omega_q\right)\mathbf{g}_B\left(\mathbf{x};\omega_q\right)\right\|}, \tag{94}$$

$$\mathbf{w}_{rA}\left(\mathbf{x};\omega_q\right) = \frac{\mathbf{g}_A\left(\mathbf{x};\omega_q\right)}{\left\|\mathbf{g}_A\left(\mathbf{x};\omega_q\right)\right\|}, \tag{95}$$

$$\mathbf{w}_{tA}\left(\mathbf{x};\omega_q\right) = \frac{\mathbf{K}_c^{-T}\left(\omega_q\right)\mathbf{g}_A\left(\mathbf{x};\omega_q\right)}{\left\|\mathbf{K}_c^{-T}\left(\omega_q\right)\mathbf{g}_A\left(\mathbf{x};\omega_q\right)\right\|}. \tag{96}$$

Proof: As noted before, from the additivity of $I(\mathbf{x})$, we can perform the optimization term by term. Also, given that each term in the sum in (90) is a product of several non negative factors, optimizing each term is equivalent to optimizing each of its factors. It follows then that we optimize each transmit and receive weight vector for each array A and B independently of each other. We consider explicitly the optimization with respect to $\mathbf{w}_{rB}\left(\mathbf{x};\omega_q\right)$. The optimization is

$$\arg \max_{\left\|\mathbf{w}_{rB}\left(\mathbf{x};\omega_q\right)\right\|=1} I(\mathbf{x}) = \arg \max_{\left\|\mathbf{w}_{rB}\left(\mathbf{x};\omega_q\right)\right\|=1} \left|\left\langle \mathbf{w}_{rB}\left(\mathbf{x};\omega_q\right), \mathbf{g}_B(\mathbf{x}_t=\mathbf{x};\omega_q)\right\rangle\right|^2. \tag{97}$$

By Schwartz inequality, (93) follows. Similarly, we obtain (94)-(96). ■

C. TRAIC-TR MUSIC

The TRAIC-TRBF forms the images by beamforming the returns from step 4 at arrays A and B, and then by triangulation of the two resulting beams. In section IV, we will compare the TRAIC-TRBF imager with other alternative imagers. One of these combines TRAIC-TR with a wideband version of the subspace based location estimation algorithm Multiple Signal Classification (MUSIC). We describe this algorithm now. The motivation to consider TRAIC-TR with MUSIC is the following: in a highly cluttered environment, where there are a large number of scatterers, MUSIC is not directly applicable. Since, intuitively, TRAIC clears the field of view by minimizing and subtracting out the clutter, it should be possible to use MUSIC after TRAIC to localize targets as long as the number of targets is smaller than the number of array elements. Because we are using wideband signals, we compute the MUSIC spectrum by combining the spectrum at all frequencies through simple multiplication of the spectrum at each frequency. We detail the method.

We perform singular value decomposition of the matrices $\mathbf{M}^B\left(\omega_q\right)$ in (84) and $\mathbf{M}^A\left(\omega_q\right)$ in (85) to

obtain

$$\mathbf{M}^B(\omega_q) = \left(\mathbf{U}_t^B(\omega_q) \;\; \mathbf{U}_n^B(\omega_q)\right) \begin{pmatrix} \mathbf{\Gamma}_t^B(\omega_q) & \mathbf{0} \\ \mathbf{0} & \mathbf{\Gamma}_n^B(\omega_q) \end{pmatrix} \left(\mathbf{V}_t^B(\omega_q) \;\; \mathbf{V}_n^B(\omega_q)\right)^H, \quad (98)$$

$$\mathbf{M}^A(\omega_q) = \left(\mathbf{U}_t^A(\omega_q) \;\; \mathbf{U}_n^A(\omega_q)\right) \begin{pmatrix} \mathbf{\Gamma}_t^A(\omega_q) & \mathbf{0} \\ \mathbf{0} & \mathbf{\Gamma}_n^A(\omega_q) \end{pmatrix} \left(\mathbf{V}_t^A(\omega_q) \;\; \mathbf{V}_n^A(\omega_q)\right)^H, \quad (99)$$

where: the $N \times r_q$ matrix $\mathbf{U}_n^B(\omega_q)$ and the $P \times r_q$ matrix $\mathbf{U}_n^A(\omega_q)$ are the left null subspaces of matrices $\mathbf{M}^B(\omega_q)$ and $\mathbf{M}^A(\omega_q)$, respectively; and r_q is the effective rank of $\mathbf{M}^B(\omega_q)$ or $\mathbf{M}^A(\omega_q)$, i.e., the number of the dominant singular values of $\mathbf{M}^B(\omega_q)$ or $\mathbf{M}^A(\omega_q)$. For example, we may define the number of dominant singular values for matrix $\mathbf{M}^B(\omega_q)$ as the minimum number of singular values whose sum exceeds

$$\tau \mathrm{Tr}\left[\mathbf{M}^B(\omega_q)\right]$$

where $0 \leq \tau \leq 1$ is close to unity (e.g., $\tau = 0.85$.) The MUSIC spectrum is computed as follows:

$$I_{\mathrm{TRMU}}(\mathbf{x}) = \frac{1}{Q} \prod_{q=0}^{Q-1} \mathcal{P}^B(\mathbf{x};\omega_q)\, \mathcal{P}^A(\mathbf{x};\omega_q), \quad (100)$$

where the factor $1/Q$ is for normalization purposes. The MUSIC spectra, at pixel $\mathbf{x}$ and frequency ω_q, $\{\mathcal{P}^B(\mathbf{x};\omega_q)\}$ and $\{\mathcal{P}^A(\mathbf{x};\omega_q)\}$ are given by

$$\mathcal{P}^B(\mathbf{x};\omega_q) = \frac{1}{\left\|\mathbf{g}_B^H(\mathbf{x};\omega_q)\,\mathbf{U}_n^B(\omega_q)\right\|^2 / \left\|\mathbf{g}_B(\mathbf{x};\omega_q)\right\|^2}, \quad (101)$$

$$\mathcal{P}^A(\mathbf{x};\omega_q) = \frac{1}{\left\|\mathbf{g}_A^H(\mathbf{x};\omega_q)\,\mathbf{U}_n^A(\omega_q)\right\|^2 / \left\|\mathbf{g}_A(\mathbf{x};\omega_q)\right\|^2}. \quad (102)$$

IV. Experimental Results

This section studies the performance of the TRAIC-TRBF imager, comparing it to TRAIC-TR MUSIC and to a conventional imager obtained by direct subtraction, as will be explained in subsection IV-B. We first measure real electromagnetic (EM) backscatter from clutters placed in the imaging area with no target, and then the EM backscatter when there are clutters *and* target(s). From these measurements, we extract the clutter channel and the clutter plus target channel frequency responses $\{\mathbf{K}_c(\omega_q), q = 0, \cdots, Q-1\}$ and $\{\mathbf{K}_{c+t}(\omega_q), q = 0, \cdots, Q-1\}$, respectively. From these we compute $\{\mathbf{K}_t(\omega_q), q = 0, \cdots, Q-1\}$. The data in steps 2 through 5 in Subsection III-A are then computer generated using these $\mathbf{K}_c(\omega_q)$ and $\mathbf{K}_t(\omega_q)$ channel responses. In other words, TRAIC-TRBF is achieved as an algorithm, with no actual retransmission of the reshaped signals. We refer to this as *mathematical* time reversal rather than *physical* time reversal, which is when we actually retransmit the time reversed signals.

We start by describing the experimental set-up and physical measurements in subsection IV-A. Subsection IV-B presents a conventional imaging method using direct subtraction (DS) beamforming (DSBF). Subsection IV-C compares the performance of four imagers for different clutter/target configurations: TRAIC-TRBF, TRAIC-TR MUSIC, DSBF, and DS MUSIC. Finally, Subsection IV-C analyzes the results to confirm that time reversal and TRAIC-TRBF improve imaging in high clutter environments.

A. Physical measurements

In this subsection, we describe successively the scattering environment, the experimental set-up, and finally the sequence of actual measurements at discrete frequencies $\omega_q, q = 0, \cdots, Q-1$ to get the clutter and the clutter plus target channel frequency response matrices $\mathbf{K}_c(\omega_q)$ and $\mathbf{K}_{c+t}(\omega_q)$, from which we get $\mathbf{K}_t(\omega_q)$.

Scattering environment. The scattering environment is illustrated in Fig. 1. It contains a number of scattering rods placed in a wood platform. The rods are a mixture of the following four types of scatterers: (1) 1.27 cm diameter ($0.5''$) copper pipe; (2) solid dielectric pipe with outer diameter of 3.2 cm, with dielectric constant 3.7; (3) dielectric rod with copper-patches to cause frequency dependent radar-cross section; and (4) extended object, 25×10 cm aluminum box. The targets are 1.3 cm diameter copper rods.

Experimental set-up. We conducted a series of electromagnetic measurements in the $4-6$ GHz frequency range, [30], uniformly sampled by $Q = 201$ frequencies. The corresponding total waveform time length is then

$$T_c = (201-1) \times \frac{1}{2 \times 10^9} = 100 \times 10^{-9}\text{s}.$$

This signal is generated by an Agilent 89610A vector signal analyzer. Both, the in-phase (I channel) and quadrature phase (Q channel) streams of the received signals are captured. Two horn antennas, both with operational bands $4-6$ GHz, are used as transmit and receive antennas. Each horn antenna is mounted on a rail and moves physically to computer controlled positions to synthesize two uniform linear arrays. In our experiments, the baseline of these arrays is limited by two factors: (1) The physical dimensions of the horn antennas set a minimum inter-element spacing of 10.16 cm; and (2) the size of the absorbing wall limits the maximum length of the transmit or receive array. This limited the two arrays to $P = N = 10$ antennas. The device noise level is set below -40 dB relative to the received signal.

Measurements. A sequence of measurements were carried out:

1) *Calibration.* The equipment, I-Q modulators, network analyzer, and horn antennas were carefully calibrated by an initial set of measurements.

2) *Clutter channel.* With the scatterers placed in their controlled positions, we measure with the I-Q modulators the response of the channel to the 201 monochromatic signals at frequencies ω_q, $q = 0, \cdots, Q-1$. The data is organized into the clutter channel frequency response matrices $\mathbf{K}_c(\omega_q), q = 0, \cdots, Q-1$.
3) *Clutter plus target channel response.* With the scatterers *and* target placed in their locations, we measure the total clutter plus target channel frequency response matrices $\mathbf{K}_{c+t}(\omega_q), q = 0, \cdots, Q-1$.

B. Conventional Imaging: Direct Subtraction (DS)

In conventional imaging, direct subtraction is commonly used to eliminate the contributions of the background and focus on objects of interest. Since from the measurements, we have both the clutter only $\mathbf{K}_c(\omega_q)$ and the clutter plus target $\mathbf{K}_{c+t}(\omega_q)$ channel frequency responses, by direct subtraction

$$\mathbf{K}_t(\omega_q) = \mathbf{K}_{c+t}(\omega_q) - \mathbf{K}_c(\omega_q). \tag{103}$$

In practice, noise and other distortions make $\mathbf{K}_t(\omega_q)$ to be different from the target channel response. Using the subspace revealing representation (15), the target response matrix $\mathbf{K}_t(\omega_q)$ is modeled as

$$\mathbf{K}_t(\omega_q) = \mathbf{g}_B(\mathbf{x}_t;\omega_q)\,\mathbf{g}_A^T(\mathbf{x}_t;\omega_q). \tag{104}$$

Direct subtraction beamformer (DSBF). The direct subtraction (DS) beamformer (DSBF) correlates the target response matrix $\mathbf{K}_t(\omega_q)$ with normalized weight vectors

$$\mathbf{w}_B(\mathbf{x};\omega_q) = \frac{\mathbf{g}_B(\mathbf{x};\omega_q)}{\|\mathbf{g}_B(\mathbf{x};\omega_q)\|}, \tag{105}$$

$$\mathbf{w}_A(\mathbf{x};\omega_q) = \frac{\mathbf{g}_A(\mathbf{x};\omega_q)}{\|\mathbf{g}_A(\mathbf{x};\omega_q)\|}, \tag{106}$$

at each frequency ω_q, which yields the DSBF image

$$I_{\mathrm{DSBF}}(\mathbf{x}) = \sum_{q=0}^{Q-1} \left| \frac{\mathbf{g}_B^H(\mathbf{x};\omega_q)\,\mathbf{K}_t(\omega_q)\,\mathbf{g}_A^*(\mathbf{x};\omega_q)}{\|\mathbf{g}_B(\mathbf{x};\omega_q)\|\,\|\mathbf{g}_A(\mathbf{x};\omega_q)\|} \right|^2. \tag{107}$$

Direct subtraction MUSIC (DS MUSIC). We can also apply MUSIC to the direct subtraction approach. By singular value decomposition

$$\mathbf{K}_{t,\mathrm{DS}}(\omega_q) = (\mathbf{U}_t(\omega_q) \;\; \mathbf{U}_n(\omega_q)) \begin{pmatrix} \mathbf{\Gamma}_t(\omega_q) & \mathbf{0} \\ \mathbf{0} & \mathbf{\Gamma}_n(\omega_q) \end{pmatrix} (\mathbf{V}_t(\omega_q) \;\; \mathbf{V}_n(\omega_q))^H, \tag{108}$$

where $\mathbf{U}_n(\omega_q)$ and $\mathbf{V}_n(\omega_q)$ define the null subspaces of matrix $\mathbf{K}_t(\omega_q)$ with r_q being its estimated rank. The DS-MUSIC spectrum is given by

$$I_{\mathrm{DSMU}}(\mathbf{x}) = \frac{1}{Q}\prod_{q=0}^{Q-1} \mathcal{J}^A(\mathbf{x};\omega_q)\mathcal{J}^B(\mathbf{x};\omega_q), \tag{109}$$

where $1/Q$ is for normalization, and

$$\mathcal{J}^B(\mathbf{x};\omega_q) = \frac{1}{\left\|\mathbf{g}_B^H(\mathbf{x};\omega_q)\,\mathbf{U}_n(\omega_q)\right\|^2 / \left\|\mathbf{g}_B(\mathbf{x};\omega_q)\right\|^2}, \quad (110)$$

$$\mathcal{J}^A(\mathbf{x};\omega_q) = \frac{1}{\left\|\mathbf{g}_A^H(\mathbf{x};\omega_q)\,\mathbf{V}_n^*(\omega_q)\right\|^2 / \left\|\mathbf{g}_A(\mathbf{x};\omega_q)\right\|^2}. \quad (111)$$

C. Test results

We now contrast the performance of the 4 imaging algorithms: (i) TRAIC+TRBF (ii) DSBF (iii) TRAIC+TR MUSIC (iv) DS MUSIC.

As mentioned at the beginning of this Section, we perform *mathematical* time reversal, rather than *physical* time reversal. In physical time reversal the data in steps 3 and 4 described in Subsection III-A are actually physically generated, transmitted, and measured. However, this is not necessary to image the target, and we can simply perform mathematical time reversal where the data in these steps is generated numerically using the channel responses $\mathbf{K}_c(\omega_q)$ and $\mathbf{K}_{c+t}(\omega_q)$ for $q = 0, \cdots, Q-1$.

We performed a battery of 11 tests with different number and configuration of clutters and targets. We report in this section the results for case 8 (17 scatterers and single target) and case 6 (6 scatterers and two targets.) Lack of space prevents detailed discussion of the other cases. Table I will summarize relevant resolution results for all 11 cases.

We show for cases 8 and 6, the images $I(\mathbf{x})$ at the output of the beamformers, see Figs. 2 through 5. These figures show the scattering configuration. For example, with respect to Fig. 2, the 17 numbers on each plate indicate the position of the scatterers. The correct position of the target is at the cross $\times$, while the peak of the image $I(\mathbf{x})$ is at the circle $\circ$. The closer the circle to the cross is, the better the localization accuracy is. The cross-range and range are in the vertical and horizontal directions, respectively, with the physical dimensions as indicated in cm along each axis. To calibrate these distances, we recall that, at the center frequency, 5 GHz, the wavelength in free space is 6 cm. The color bar on the side shows the dB scale starting from 0 dB at the top (dark blue in color printing.) For each image, the total range of the color bar shows the dynamic range of the imager. For visual comparison purpose, the images in Figs. 2 and 4 are properly scaled to the same range in dB. The sharper high contrast images provide better details, and thus better resolution.

17 Scatterers and 1 target. The templates in Fig. 2, from top to bottom, left to right, show the TRAIC+TRBF, DSBF, TRAIC-TR MUSIC, and DS MUSIC images. Fig. 3 shows the projections along the cross-range (left template) and range (right template) of the 3D $I(\mathbf{x})$ for the TRAIC-TRBF (heavy trace with x) and the DSBF (lighter trace).

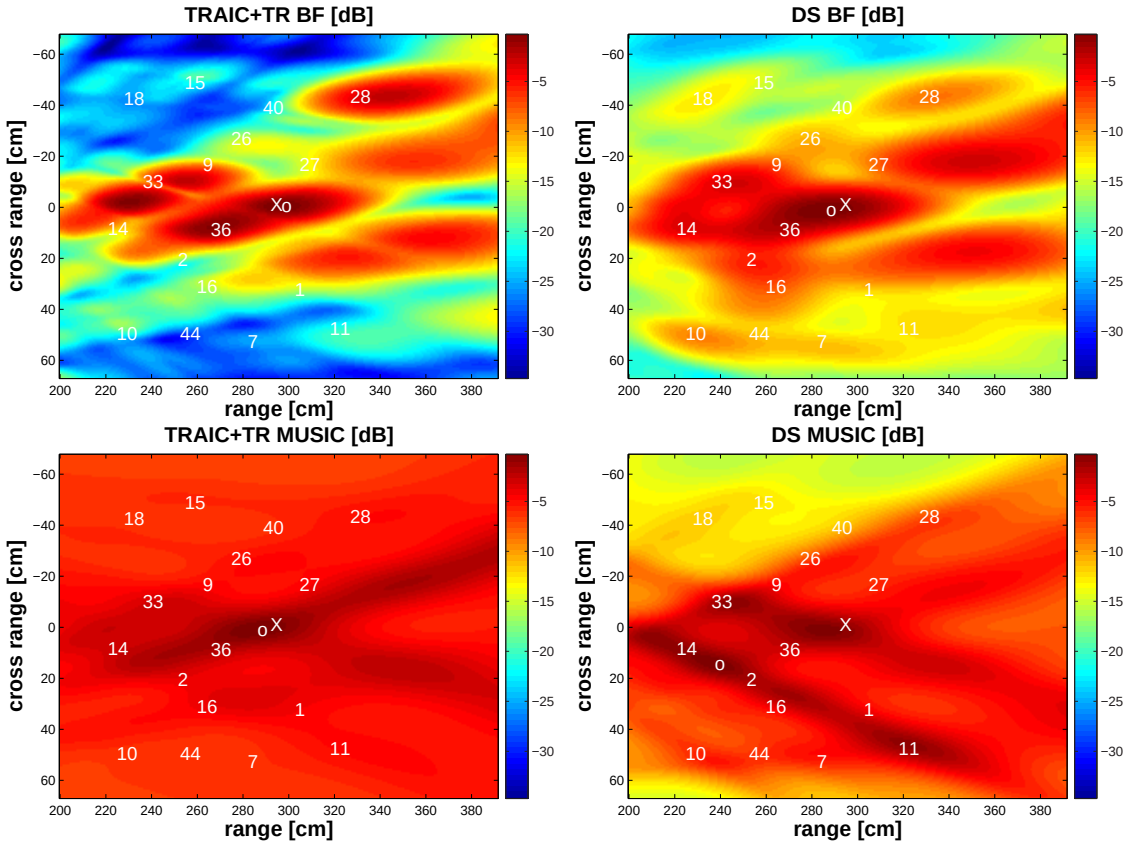

Fig. 2. Time Reversal imaging with 17 scatterers and 1 target. Numbers indicate locations of the scatterers, $\times$ and $\circ$ indicate the exact location of the target and the peak value of the image, respectively. Top left–TRAIC+TRBF. Top right–DSBF. Bottom left–TRAIC+TR MUSIC. Bottom right–DS MUSIC. All images are plotted within the same range ($0 \sim -34$ dB).

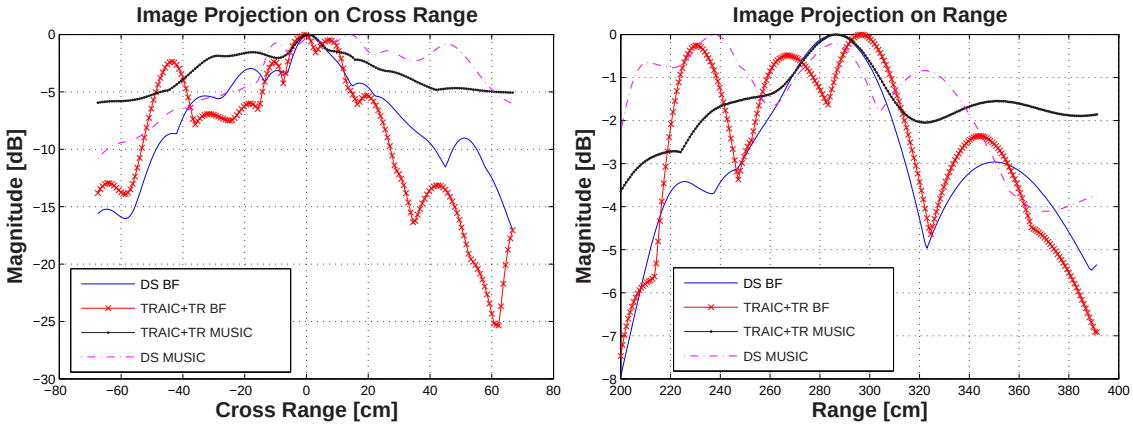

Fig. 3. The projection onto cross range and range for the images in Fig. 2. Left–Cross range; Right–Range. TRAIC shows a narrower main lobe, deeper null, and lower sidelobes relative to direct subtraction imaging.

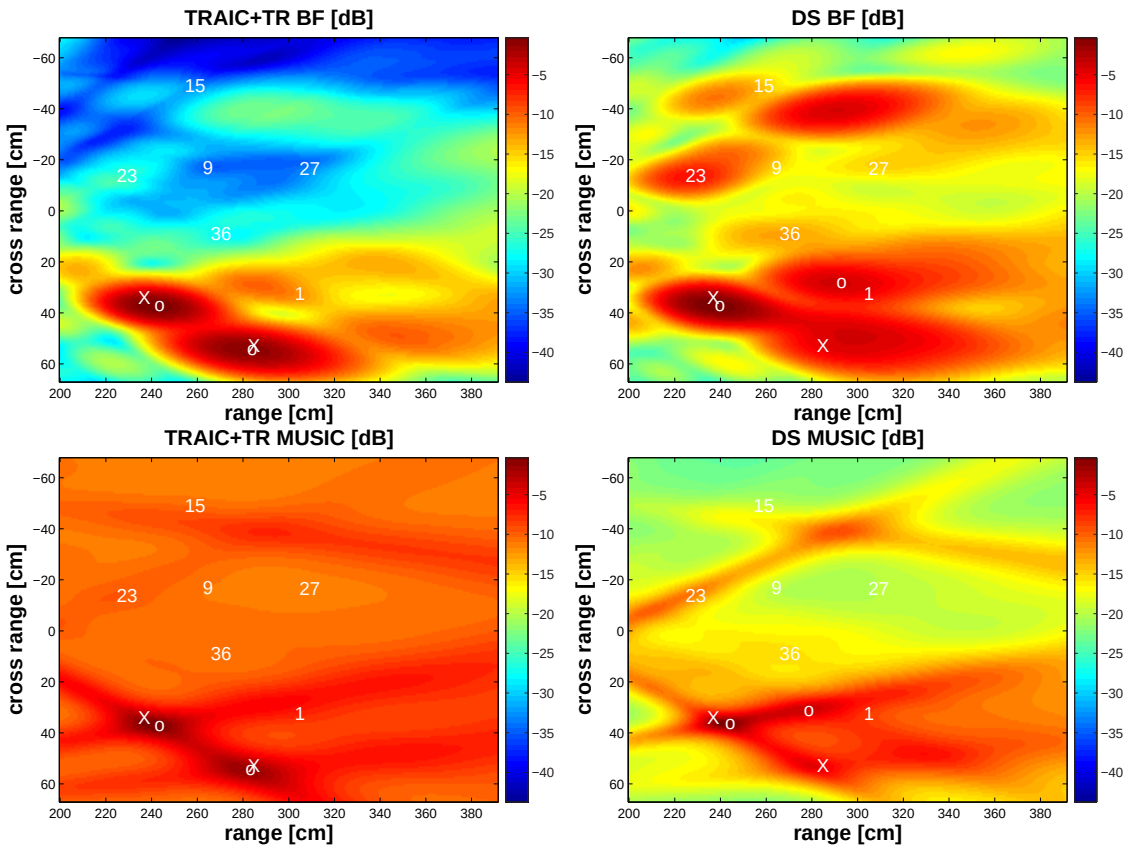

Fig. 4. Time Reversal imaging with 6 scatterers and 2 targets. Numbers indicate locations of the scatterers, $\times$ and $\circ$ indicates the exact location of the target and the peak value of the image, respectively. Top left–TRAIC+TR beamforming. Top right–Direct subtraction beamforming. Bottom left–TRAIC+TR MUSIC. Bottom right–Direct subtraction MUSIC. All images are plotted within the same range ($0 \sim -45$ dB).

There are a number of important remarks from Figures 2 and 3 that demonstrate the higher cross-range and range resolution provided by TRAIC-TRBF over all the other alternative algorithms. The first is the dynamic range that is about 35 dB for TRAIC-TRBF, 10 dB larger than for DSBF, and about 20 dB larger than for the MUSIC based algorithms. The higher resolution of TRAIC-TRBF is also apparent from Figure 2, where the lobe around the target is narrower in both (cross-range and range) directions. Both points are also well made with Figure 3: the higher resolution is apparent from much narrower main lobes and the dynamic range is a result of smaller sidelobes. Furthermore, in this case, the number of antennas ($= 10$) is smaller than the number of scatterers ($= 17$). The resulting images using TRAIC demonstrate that TRAIC successfully mitigates the clutters' response and focuses on the intended target.

6 Scatterers and 2 targets. Fig. 4 depicts the images formed by the same 4 algorithms now using case 6 with a total of 6 scatterers and 2 targets. The top left panel shows that the TRAIC-TRBF mitigates

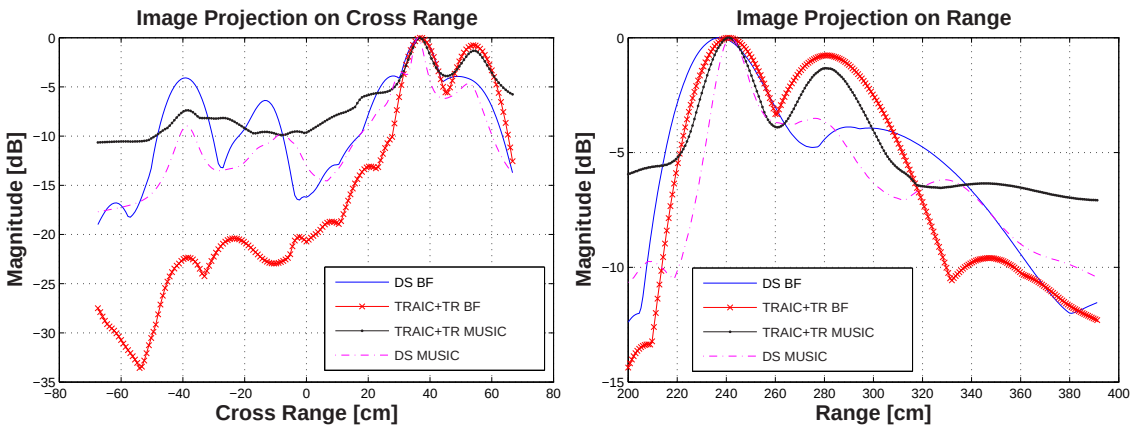

Fig. 5. The projection onto cross range and range for the formed image in Fig. 4. Left–Cross range projection. Right–Range projection. TRAIC+TRBF yields two lobes corresponding to two target locations.

the clutter (scatterers $9, 15, 27, 23, 36$ are placed in deep nulls) and focuses on both targets. The dynamic range is about 45 dB, compared with about 30 dB dynamic range for the DSBF, 11 dB for TRAIC-TR MUSIC and 22 dB for DS MUSIC. Both, the DSBF and the DS MUSIC, miss the target at range 290 cm. Fig. 5 shows the projection of the TRAIC-TRBF and DSBF images onto cross-range and range. The left image clearly shows two high peaks for TRAIC+TR beamforming. We observe a -5 dB null between the two peaks. For the direct subtraction beamforming, the second peak misses the target completely.

Resolution. We consider the two dimensional point spread function (PSF) of the imager, which is its output when the targets are pointwise. The PSF is

$$I\left(\mathbf{x},\overline{\mathbf{x}}\right)=\sum_{q=0}^{Q-1}\left|\mathbf{w}_{rB}^{H}\left(\mathbf{x};\omega_q\right)\mathbf{M}^{B}\left(\overline{\mathbf{x}},\omega_q\right)\mathbf{w}_{tB}\left(\mathbf{x};\omega_q\right)\right|^2\left|\mathbf{w}_{rA}^{H}\left(\mathbf{x};\omega_q\right)\mathbf{M}^{A}\left(\overline{\mathbf{x}},\omega_q\right)\mathbf{w}_{tA}\left(\mathbf{x};\omega_q\right)\right|^2, \quad (112)$$

where $\overline{\mathbf{x}}$ is the actual source location and $\mathbf{x}$ is the pixel location on which the transmit and receive beams focus. Define $\Delta\mathbf{x}=\mathbf{x}-\overline{\mathbf{x}}$, and

$$\widetilde{\mathbf{J}}\left(\mathbf{x}\right)=\frac{1}{I\left(\overline{\mathbf{x}}\right)}\mathbf{J}\left(\mathbf{x}\right)=-\frac{1}{I\left(\overline{\mathbf{x}}\right)}\frac{\partial}{\partial\mathbf{x}}\left(\frac{\partial}{\partial\mathbf{x}}I\left(\mathbf{x}\right)\right)^{T}\Bigg|_{\mathbf{x}=\overline{\mathbf{x}}}. \quad (113)$$

Second order Taylor's series expansion about $\overline{\mathbf{x}}$ of the PSF leads to

$$I\left(\mathbf{x},\overline{\mathbf{x}}\right)\approx 1-\frac{1}{2}\left(\Delta\mathbf{x}\right)^{T}\mathbf{J}\left(\mathbf{x}\right)\left(\Delta\mathbf{x}\right), \quad (114)$$

The diagonal elements of the inverse $\widetilde{\mathbf{J}}(\mathbf{x})^{-1}$, i.e., $\widetilde{\mathbf{J}}^{-1}\left(\mathbf{x}\right)_{xx}$ and $\widetilde{\mathbf{J}}^{-1}\left(\mathbf{x}\right)_{yy}$, evaluated at the peak of the beamformed images are a measure of how narrow or wide the main lobe is. In other words, these values provide a quadratic description of the main lobe of (112). The analytical expression (113) is hard to obtain due to its complexity. We resort to numerical means by finite difference replacement of the

	TRAIC+TRBF $(\widetilde{\mathbf{J}}^{-1})_{yy}$	DSBF $(\widetilde{\mathbf{J}}^{-1})_{yy}$	TRAIC+TRBF $(\widetilde{\mathbf{J}}^{-1})_{xx}$	DSBF $(\widetilde{\mathbf{J}}^{-1})_{xx}$	TRAIC+TRBF $(\widetilde{\mathbf{J}}^{-1})_{xy}$	DSBF $(\widetilde{\mathbf{J}}^{-1})_{xy}$
Case-1	12.4	23.1	144.4	246.0	7.2	19.2
Case-2	12.5	27.2	129.5	278.4	15.3	35.2
Case-3	34.5	96.0	339.4	359.7	-42.8	-103.2
Case-4	13.3	21.0	131.0	194.2	4.6	6.0
Case-5	22.3	33.2	233.8	354.6	31.7	62.8
Case-6	19.5	36.0	218.5	421.3	22.5	79.6
	55.6	88.4	766.2	1186.7	138.3	101.8
Case-7	85.5	121.8	1225.8	1103.7	256.4	-163.0
	108.2	52.5	1273.4	780.0	-333.7	-138.8
Case-8	16.0	45.0	289.7	759.1	-17.6	-94.9
Case-10	15.1	22.9	150.6	200.0	6.3	5.9
Case-13	24.9	29.8	256.9	338.3	43.5	55.1
	165.2	258.2	2271.8	4395.4	430.9	770.8
Case-14	22.8	39.5	199.6	403.8	44.8	91.1

TABLE I

RANGE RESOLUTION (x) AND CROSS RANGE RESOLUTION (y) FOR TRAIC+TRBF AND DSBF

second derivatives $\frac{\partial^2}{\partial x^2}\left[I\left(\mathbf{x}\right)\right]_{i,j}$, $\frac{\partial 2}{\partial y^2}\left[I\left(\mathbf{x}\right)\right]_{i,j}$ and the mixed derivative $\frac{\partial^2}{\partial x \partial y}\left[I\left(\mathbf{x}\right)\right]_{i,j}$ as approximations, defined as follows: [31]

$$\left.\frac{\partial^2 I_{i,j}}{\partial x^2}\right|_{i,j} = \frac{I_{i+1,j} - 2I_{i,j} + I_{i-1,j}}{\Delta^2} + O(\Delta^2) \tag{115}$$

$$\left.\frac{\partial^2 I_{i,j}}{\partial y^2}\right|_{i,j} = \frac{I_{i,j+1} - 2I_{i,j} + I_{i,j-1}}{\Delta^2} + O(\Delta^2) \tag{116}$$

$$\begin{aligned}\left.\frac{\partial^2 I_{i,j}}{\partial x \partial y}\right|_{i,j} = {} & \frac{1}{4\Delta^2}\left\{3\left[I_{i+1,j+1} + I_{i-1,j-1}\right] - \left[I_{i-1,j+1} + I_{i+1,j-1}\right]\right. \\ & \left. -2\left[I_{i+1,j} + I_{i,j+1} + I_{i-1,j} + I_{i,j-1} - 2I_{i,j}\right]\right\} + O(\Delta^2)\end{aligned} \tag{117}$$

where $I_{i,j} = I\left(x_i, y_j\right)$. Eqn. (117) uses a nine point numerical approximation to the cross second order derivative. Because $\Delta = 0.75$ cm, the grid size is sufficiently small to ensure the smoothness of the numerical solution. Table I shows these quantities for all 11 cases studied. They show that, except for one of the targets in case 7, the main lobe of the TRAIC-TRBF image is consistently narrower than the main lobe of the DSBF along both the range and cross range directions.

Discussion The proposed TRAIC+TR BF algorithm images a target scene using mathematical time

reversal twice. The first time reversal step nulls the clutter; the second time reversal step focuses on the target. The target data matrix defined in (19), in dense scattering, contains both the direct reflection between the target and the receive array, *and* the secondary reflections between the scatterers, the target, and the receive array. The clutter nulling step suppresses the clutter reflections, *not* the secondary scattering between the target, the scatterers, and the receiver. The target focusing step back propagates the wave field and focuses on the target. After the target focusing step, the measurements contain the energy focused wavefield; then, we apply a beamformer weight vector to locate the target.

Because the focused wavefield contains direct and secondary scattering, ideally, the weight vector, i.e., the field Green's function, should combine the direct reflection from the target to the receiver, and the secondary scattering due to the presence of the surrounding scatterers. In our algorithm, we use only the direct path Green's function, which, in a sense, is equivalent to the Born approximation [16]. This avoids having to locate the scatterers, which is challenging in high scattering environments. But, high scattering environment is exactly where time reversal makes a difference, and so, our method of nulling the scatterers before focusing on the targets, avoids having to resolve the scatterers, still providing good target imaging performance. This simplification, however, may explain why, in the experiment with 17 scatterers and 1 target, reported in Fig. 2, some local maxima are close to the global maxima.

The effect of multiple scattering on time reversal imaging has been studied in [15], [16], [17], where the Foldy-Lax model [32] is employed. For example, references [16], [17] show that, despite the presence of non-negligible multiple scattering, the time reversal imaging with MUSIC works well in predicting the scatterers' locations. However, MUSIC is limited by the condition that the number of antennas is larger than the number of scatterers, which is common in heavy scattering environments. Another example of using the Foldy-Lax model is the maximum likelihood estimation of point scatterers reported in [15], where the locations of the scatterers and their reflectivity coefficients are estimated iteratively through the maximum likelihood approach. That is, starting from an initial estimate of the target location and updating the estimates iteratively by optimizing a chosen non-linear cost function, the algorithm in [15] generates an image of all the scatterers. However, all the examples shown in [15] use a number of antennas that is significantly larger than the number of scatterers plus targets, for example, 40 antennas or 8 antennas and 3 scattering objects (scatterers plus targets). Other than MUSIC, [26] implements a high dimensional signal subspace localization method. In contrast, our proposed algorithm does not attempt to estimate the locations of the clutters (i.e., the unwanted scatterers) explicitly, rather it suppresses the clutter and then focuses on the targets. This strategy avoids the problem of directly estimating the parameters of the clutter, which may be an impossible task when the number of clutters is very large. For example, we show results when using 10 antennas and 17 scatterers.

In terms of the computational complexity, our proposed TRAIC+TR BF algorithm is comparable to the conventional DS BF algorithm. For simplicity, we assume that the number of antennas in array A and B are the same ($N = P$), and that we do not consider the unit normalization constraint in the weight vectors (93)-(96) and (105)-(106) for the moment. Using the Big-O notation, we can show that the DS BF algorithm has the computational complexity $O(J_x J_y Q(2N^2 + 2N)) = O(J_x J_y Q N^2)$, where N is the size of the weight vectors and the data matrices, Q is the number of frequencies, J_x and J_y are the number of pixels in range and cross range, respectively; similarly, the TRAIC+TR BF algorithm has the computational complexity $O(J_x J_y Q 16N^2 + QcN^3)$, where the factor N^3 results from inverting the matrices $\mathbf{K}_c(\omega_q)$, and c is a small constant. In our experiments, we choose $N = 10, Q = 201, J_x = 256, J_y = 200$, so the numbers Q, J_x, J_y are dominant with respect to N. Thus, the computational complexity of the TRAIC+TR BF is still comparable to that of the DS BF for a large Q, J_x, J_y, and smaller N. This conclusion still holds when the computation of the unit normalization constraint is taken into account in that the number of operations of carrying out the unit normalization for both algorithms is on the order of $O(J_x J_y Q N)$.

Another important question is the effect of measurement noise. In this paper, we rely on experimental data for algorithm verification. The noise power in the collected experimental data is low relative to the signal and clutter power. The device noise is measured experimentally to be below -40 dB relative to the received signal. The analysis of the noise effect on the time reversal imaging algorithm proposed here will be reported elsewhere. Interested readers can refer to [33] where the impact of noise on time reversal detection is analyzed.

V. Conclusion

In this paper we present a new high resolution radar imaging system to detect and locate targets using time reversal in rich scattering environments, where the number of scatterers is significantly larger than the number of antennas. The proposed imaging system performs two major tasks by time reversal: clutter mitigation and target focusing. Clutter mitigation is accomplished by a *Time Reversal Adaptive Interference Canceler* (TRAIC) through waveform reshaping to null out the clutters. After clutter is suppressed and subtracted out, a second time reversal for target focusing is performed. A final image is then obtained by beamforming. A series of experimental tests in electromagnetic domain have demonstrated the good performance of the proposed imaging algorithm over conventional approaches. In future research, we intend to pursue performance analysis studies of the TRAIC time reversal beamformer and find ways of handling explicitly the secondary scattering between scatterers and targets, while avoiding resolving the individual scatterers. We are also currently extending our imaging algorithm to synthetic aperture monostatic and bistatic radar, see [34] for some preliminary results.

REFERENCES

[1] A. B. Baggeroer, W. A. Kuperman, and P. N. Mikhalevsky, "An overview of matched field methods in ocean acoustics," *IEEE J. of Oceanic Engineering*, vol. 18, no. 4, pp. 401–424, April 1983.

[2] M. Fink, C. Prada, F. Wu, and D. Cassereau, "Self focusing in inhomogeneous media with time reversal acoustic mirrors," in *IEEE Ultrasonics Symposium*, vol. 1. Montreal, Canada: IEEE, NJ, 1989, pp. 681–686.

[3] C. Prada, F. Wu, and M. Fink, "The iterative time reversal mirror: A solution to self-focusing in the pulse echo mode," *J. Acoustic Society of America*, vol. 90, pp. 1119–1129, 1991.

[4] M. Fink, "Time reversal of ultrasonic fields. Part I: Basic principles," *IEEE Transactions on Ultrasonic, Ferroelectronic, and Frequency Control*, vol. 39, no. 5, pp. 555–566, September 1992.

[5] ——, "Time reversed acoustics," *Physics Today*, vol. 50, no. 3, pp. 34–40, 1997.

[6] M. Fink, D. Cassereau, A. Derode, C. Prada, P. Roux, M. Tanter, J.-L. Thomas, and F. Wu, "Time-reversed acoustics," *Reports on Progress in Physics*, vol. 63, no. 12, pp. 1933–1995, December 2000.

[7] W. A. Kuperman, W. S. Hodgkiss, and H. C. Song, "Phase conjugation in the ocean: Experimental demonstration of an acoustic time-reversal mirror," *J. Acoustic Society of America*, vol. 103, no. 1, pp. 25–40, January 1998.

[8] H. C. Song, W. A. Kuperman, W. S. Hodgkiss, T. Akal, and C. Ferla, "Iterative time reversal in the ocean," *J. Acoustic Society of America*, vol. 105, no. 6, pp. 3176–3184, June 1999.

[9] B. E. Henty and D. D. Stancil, "Multipath enabled super-resolution for RF/microwave communication using phase-conjugate arrays," *Physical Review Letters*, vol. 93, no. 24, p. 243904, December 2004.

[10] S. K. Lehman and A. J. Devaney, "Transmission mode time-reversal super-resolution imaging," *J. Acoustic Society of America*, vol. 113, no. 5, pp. 2742–53, May 2003.

[11] A. J. Devaney, "Time reversal imaging of obscured targets from multistatic data," *IEEE Transaction on Antennas and Propagation*, vol. 53, no. 5, pp. 1600–1610, May 2005.

[12] C. Prada and J.-L. Thomas, "Experimental subwavelength localization of scatterers by decomposition of the time reversal operator interpreted as a covariance matrix," *J. Acoust. Soc. Am.*, vol. 114, no. 1, pp. 235–243, July 2004.

[13] L. Borcea, G. Papanicolaou, C. Tsogka, and J. Berryman, "Imaging and time reversal in random media," *Inverse Problems*, vol. 18, pp. 1247–1289, 2002.

[14] C. Oestges, A. D. Kim, G. Papanicolaou, and A. J. Paulraj, "Characterization of space time focusing in time reversed random fields," *IEEE Transactions on Antennas and Propagation*, vol. 53, no. 1, pp. 283–293, January 2005.

[15] G. Shi and A. Nehorai, "Maximum likelihood estimation of point scatterers for computational time-reversal imaging," *Communications in Information and Systems*, vol. 5, no. 2, pp. 227–256, 2005.

[16] A. J. Devaney, E. A. Marengo, and F. K. Gruber, "Time-reversal-based imaging and inverse scattering of multiply scattering point targets," *J. Acoust. Soc. Am.*, vol. 118, no. 5, pp. 3129–3138, November 2005.

[17] F. K. Gruber, E. A. Marengo, and A. J. Devaney, "Time-reversal imaging with multiple signal classification considering multiple scatering between the targets," *J. Acoust. Soc. Am.*, vol. 115, no. 6, pp. 3042–3047, June 2004.

[18] J. M. F. Moura and Y. Jin, "Detection by time reversal: Single antenna," *IEEE Transactions on Signal Processing*, vol. 54, no. 12, December 2006, accepted for publication on February 2006.

[19] A. V. Oppenheim, A. S. Willsky, and S. H. Nawab, *Signals & Systems, 2nd edition*. Upper Saddle River, NJ: Prentice-Hall, Inc., 1996.

[20] D. R. Wehner, *High Resolution Radar*. Norwood, MA: Artech House, 1994.

[21] B. R. Mahafza and A. Z. Elsherbeni, *MATLAB Simulations for Radar System Design*. Baco Raton, FL: CRC Press, 2003.

[22] A. J. Devaney, "Using field correlations to estimate Green's functions from experimental data," 2004, (Unpublished manuscript.).

[23] D. H. Chambers and J. G. Berryman, "Analysis of the time reversal operator for a small spherical scatterer in an electromagnetic field," *IEEE Transactions on Antennas and Propagation*, vol. 52, no. 7, pp. 1729–1738, July 2004.

[24] R. E. Jorgenson and R. Mittra, "Efficient calculation of the free space periodic Green's function," *IEEE Transactions on Antennas and Propagation*, vol. 38, no. 5, pp. 633–642, May 1990.

[25] P. M. Morse and H. Feshback, *Methods of Theoretical Physics, Part I*. New York, NY: McGraw-Hill, 1953.

[26] E. A. Marengo and F. K. Gruber, "Subspace-based localization and inverse scattering of multiply scattering point targets," *EURASIP Journal on Advances in Signal Processing*, vol. 2007, pp. Article ID 17 342, 16 pages, 2007.

[27] J. M. F. Moura, Y. Jin, D. Stancil, J. Zhu, A. Cepni, Y. Jiang, and B. Henty, "Single antenna time reversal adaptive interference cancelation," in *ICASSP'05, IEEE International Conference on Signal Processing*, vol. IV. Philadelphia, PA: IEEE, March 2005, pp. 1121–1124.

[28] S. Boyd, L. E. Ghaoui, E. Feron, and V. Balakrishnan, *Linear Matrix Inequalities in System and Control Theory*. Philadelphia, PA: SIAM Studies in Applied Mathematics, 1994.

[29] R. A. Horn and C. R. Johnson, *Matrix Analysis*. New York: Cambridge University Press, 1985.

[30] A. Cepni, "Experimental investigation of time-reversal techniques using electromagnetic waves," Ph.D. dissertation, Carnegie Mellon University, Department of Electrical and Computer Engineering, December 2005.

[31] A. R. Mitchell and D. F. Griffiths, *The Finite Difference Method in Partial Differential Equations*. New York, NY: John Wiley & Sons, 1980.

[32] R. K. Snieder and J. A. Scales, "Time-reversal imaging as a diagnostic of wave and particle chaos," *Physical Review E*, vol. 58, no. 5, pp. 5668–5675, November 1998.

[33] Y. Jin and J. M. F. Moura, "Asymptotic noise analysis of time reversal detection," in *The 40th Asilomar Conference on Signals, Systems and Computers 2006*. Pacific Grove, CA: IEEE, Oct. 29 - Nov. 1, 2006.

[34] ——, "TR-SAR: Time reversal target focusing in synthetic aperture radar," in *IEEE International Conference on Acoustics, Speech and Signal Processing, ICASSP'07*, vol. 2. Honolulu, HI: IEEE, April 2007, pp. 957–960.